HHS Public Access

Author manuscript

Clin Cancer Res. Author manuscript; available in PMC 2022 August 23.

Published in final edited form as:

Clin Cancer Res. 2020 June 01; 26(11): 2582–2594. doi:10.1158/1078-0432.CCR-19-3717.

Predicting Therapeutic Antibody Delivery into Human Head and Neck Cancers

Guolan Lu[1], **Shayan Fakurnejad**[2], **Brock A. Martin**[3], **Nynke S. van den Berg**[1], **Stan van Keulen**[1], **Naoki Nishio**[1], **Ashley Zhu**[1], **Stefania U. Chirita**[1], **Quan Zhou**[1], **Rebecca Gao**[2], **Christina S. Kong**[3], **Nancy Fischbein**[4], **Mrudula Penta**[4], **Alexander D. Colevas**[5], **Eben L. Rosenthal**[1,4]

[1]Department of Otolaryngology – Head and Neck Surgery, Stanford University, Stanford, California, 94305

[2]Stanford University School of Medicine, Stanford, California, 94305

[3]Department of Pathology, Stanford University, Stanford, California, 94305

[4]Department of Radiology, Stanford University, Stanford, California, 94305

[5]Department of Medicine, Division of Oncology, Stanford University, Stanford, California, 94305

Abstract

Purpose: The efficacy of antibody-based therapeutics depends on successful drug delivery into solid tumors, therefore there is a clinical need to measure intratumoral antibody distribution. This study aims to develop and validate an imaging and computation platform to directly quantify and predict antibody delivery into human head and neck cancers in a clinical study.

Experimental Design: Twenty-four patients received systemic infusion of a near-infrared (NIR) fluorescence-labeled therapeutic antibody followed by surgical tumor resection. A computational platform was developed to quantify the extent of heterogeneity of intratumoral antibody distribution. Both univariate and multivariate regression analysis were used to select the most predictive tumor biological factors for antibody delivery. Quantitative image features from the pre-treatment magnetic resonance imaging (MRI) were extracted and correlated with fluorescence imaging of antibody delivery.

Results: This study not only confirmed heterogeneous intratumoral antibody distribution in line with many preclinical reports, but also quantified the extent of inter-patient, inter-tumor, and intra-tumor heterogeneity of antibody delivery. This study demonstrated the strong predictive value of tumor size for intratumoral antibody accumulation and its significant impact on antibody distribution in both primary tumor and lymph node metastasis. Furthermore, this study established the feasibility of using contrast-enhanced MRI to predict antibody delivery.

Corresponding author: Eben L. Rosenthal, MD, Professor of Otolaryngology and Radiology, Ann & John Doerr Medical Director, Stanford Cancer Center, 900 Blake Wilbur Dr, CA 94305, 205-996-5009 (p), (650) 724-1458 (f), elr@stanford.edu .

Conflict of interest disclosure statement: Eben Rosenthal is a consultant for LICOR Biosciences that manufactures IRDye800 and has equipment loans from this company. Other authors report no conflicts of interest.

Conclusions: This study provides a clinically translatable platform to measure antibody delivery into solid tumors and yields valuable insight into clinically relevant antibody tumor penetration, with implications in the selection of patients amenable to antibody therapy and the design of more effective dosing strategies.

Keywords

antibody delivery; head and neck cancers; fluorescence; MRI; early-phase clinical trial

Introduction

Heterogeneous patient response to antibody-based therapeutics remains a major challenge in drug discovery and patient care, especially in oncology and immune therapy (1,2). Although genomics is sought to predict therapeutic response, limited success has been achieved (3). An important but often neglected aspect is the measurement of intratumoral antibody concentration and distribution (4,5), which could guide precision dosing and select patients with high drug accumulation and thus more likely to respond to therapies (6–8). Current early phase clinical trials routinely use plasma drug concentrations as a surrogate to guide dose optimization (9,10), which assumes homogenous intratumoral antibody distribution and may lead to suboptimal response and resistance (5). Therefore, quantification and prediction of intratumoral antibody delivery remain a critically unmet need in the clinic.

Since understanding variability and biological correlates of antibody delivery in humans are not part of drug development routine, our current knowledge on intratumoral antibody distribution and the underlying biological mechanism has largely originated from preclinical studies (4,11–18), which has shown low and heterogeneous antibody delivery into solid tumors. To be effective, systemic anti-cancer agents must extravasate across blood vessels and diffuse through the interstitial space before binding to its cellular target in optimal concentrations. Based on this biophysical process, preclinical studies have hypothesized several barriers to drug transport, including reduced vascular density and disorganized vascular architecture (4,19), complex composition and structure of the extracellular matrix (20,21), antigen expression levels (22,23), and sub-optimal antibody dosing (24). Given the large gap between preclinical efficacies of antibodies and the clinical outcomes (25,26), it is imperative to directly measure antibody delivery and verify these hypothesis in human patients.

Although positron emission tomography (PET) imaging of radiolabeled antibodies is an important clinical approach to evaluate the whole-body antibody distribution at the organ level non-invasively (27–30), this approach is limited by its high cost, inevitable radiation, and insufficient resolution (1~2 mm) (27). With the advent of fluorescently labeled antibodies under good manufacturing practice suitable for patient injection (31,32), it is now possible to use high-resolution fluorescence imaging to complement organ-level PET imaging to measure intratumoral antibody distribution and cellular antibody binding and to correlate with tumor microenvironment factors (5,27).

In this study, we proposed a clinically applicable imaging and computation platform that integrated pretreatment contrast-enhanced magnetic resonance imaging (MRI) and

a fluorescently labeled therapeutic antibody to measure and predict antibody delivery into solid tumors. We systemically administered an anti-epidermal growth factor receptor (EGFR) antibody (approved anti-cancer drug by the U.S. Food and Drug Administration (FDA)) conjugated with a near-infrared (NIR) fluorophore (panitumumab-IRDye800CW) into 24 patients with head and neck squamous cell carcinoma (HNSCC). Using surgical specimens from these patients, we attempted to quantify the extent of heterogeneity in antibody distribution within human tumors, to assess the impact of tumor biological parameters on intratumoral antibody delivery into human tumors, and to evaluate the feasibility of using contrast-enhanced MRI to predict antibody delivery into human solid tumors.

Materials and Methods

Clinical Study Overview

Fig. 1 illustrated an overview of the study design. First, patients received the standard-of-care MRI scan (including the contrast-enhanced T1-weighted imaging sequence). Next, patients were enrolled into a surgical-window trial in which varying doses (25–95mg) of panitumumab-IRDye800 were intravenously infused several days before curative resection of 24 patients with HNSCC (Table S1, Clinicaltrials.gov Identifier: NCT02415881). Fresh tissue samples from the primary tumor specimen were collected to measure antibody concentration in tissue. The macroscopic antibody distribution was quantified in 5 mm thick formalin-fixed tumor specimens, while the mesoscopic and microscopic antibody distribution were quantified in formalin-fixed paraffin-embedded (FFPE) tissue. The fluorescent antibody distribution through the whole-tumor specimens were then correlated back to the imaging features extracted from the contrast-enhanced T1-weighted MRI. Finally, the impact of tumor biological variables on intratumoral antibody delivery was assessed using an automated image analysis pipeline for the serial tissue sections of tumor markers (Fig. 1B, Fig. S1). The study protocol was approved by the Stanford University Institutional Review Board (IRB). Following IRB approval, the study was conducted in accordance with the Helsinki Declaration of 1975 and its amendments, FDA's ICH-GCP guidelines, and the laws and regulations of the United States. Written informed consent was obtained from all patients.

Quantitation of Panitumumab-IRDye800 Concentration in Fresh Tissue Specimen

To measure the concentration of panitumumab-IRDye800 in patient samples, tumor or normal tissue were first disrupted with a homogenizer using chilled lysis buffer (50 mM Tris-HCl pH 7.4, 150 mM NaCl, 1 mM EDTA, 1% Triton X-100, 0.1% SDS) containing a protease inhibitor (Roche, Indianapolis, IN). Next, a standard curve was produced by adding known amounts (0–5 ng/μl) of panitumumab-IRDye800 into three replicates of control tissue homogenates from non-infused patients in a 96-well half-area black plate. Then, 100 μl of the tumor, muscle, and skin homogenates from study patients were also added into individual wells of the same 96-well plate for measurement by a NIR plate reader (Tecan, Zürich, Switzerland). Subsequently, the concentration of the antibody-dye in the tissue homogenates was extrapolated from the standard curve. The final concentrations of antibody-dye were normalized by tissue weight and reported as ng/mg of tissue.

NIR Fluorescence Imaging of Panitumumab-IRDye800

Macroscopic imaging: Primary tumor specimens were formalin-fixed overnight and sectioned into 5 mm sections that were imaged with a macroscopic NIR fluorescence imager (the Pearl Trilogy imaging system, LI-COR Biosciences, Lincoln, NE USA). These tissues were subsequently formalin-fixed paraffin embedded following standard pathological workflow.

Mesoscopic imaging: Representative FFPE tissue blocks were cut into 5 μm serial tissue slices for the primary tumor or 4 μm serial tissue slices for lymph nodes. These tissue slides were baked for 1 hour at 60 ^{o}C and then imaged using a mesoscopic NIR fluorescence imager (the Odyssey CLx imaging platform, LI-COR Biosciences, Lincoln, NE USA).

Microscopic imaging: Subsequently, one of the serial tissue sections was deparaffinized and stained with 4′, 6-diamidino-2-phenylindole (DAPI) for imaging under a customized NIR fluorescence microscope (Leica Microsystems Inc. Chicago, IL). The imaging system is a fully automated upright microscope mainly consisting of a scientific CMOS fluorescence camera, multiple fluorescence filter cubes, a motorized XYZ scanning stage, and a LAS X software workstation. This system is capable of simultaneous imaging of multiple fluorescence channels, including DAPI: 480nm/527nm, and NIR: 774nm/789nm. The title scan function was used to scan the entire tumor sections section at a resolution of 1.3μm/pixel and stitched adjacent image fields into a single large mosaic image for subsequent analysis.

Histopathology and Immunohistochemistry

One of the serial tissue sections was stained with hematoxylin and eosin (H&E) and reviewed by an experienced pathologist to outline tumor boundaries and identify cancerous regions. The remaining serial sections were prepared for Masson's trichrome staining (collagen) and immunohistochemistry (IHC) staining of EGFR, ERG, and α-SMA. More details can be found in the supplementary method. All the slides were digitally scanned at 20× magnification into whole-slide digital images using a NanoZoomer scanner (Hamamatsu, Japan).

Quantitative Fluorescence Image Analysis

To quantify antibody uptake and distribution on macroscopic images, tumor boundaries outlined on digital whole-slide images of H&E staining were mapped back to corresponding tissue breadloafs, and all the breadloafs were stacked back together to reconstruct the original primary tumor specimen. Similarly, tumor regions within metastatic lymph nodes were also identified. Next, the fluorescence intensities within the tumor region of all the breadloafs were extracted to compute the first-order statistical quantifying antibody uptake (mean fluorescence intensity (MFI)) and distribution heterogeneity (entropy, standard deviation, uniformity, variance), as well as Haralick texture features (correlation, difference entropy, difference variance, homogeneity, information measure of correlation) (33).

Next, a quantitative image analysis pipeline (Fig. 1B) was developed to quantify sets of serial whole-slide digital images of H&E, Masson's Trichrome, EGFR, ERG, α-SMA,

and fluorescence microscopic images. This pipeline encompassed four steps. The first step was to co-localize the antibody distribution with all the molecular markers within the tumor region. This was done by co-registering fluorescence microscopic images with H&E, Masson's trichrome, and IHC images using a semi-automated control-point based rigid registration algorithm. Whole-slide digital images were downsized from 20× magnification to 5× to facilitate fast computing during registration. The second step was to map tumor boundaries extracted from H&E images onto all the other images. Regions with artifacts on fluorescence images were excluded from the tumor region. The third step was done by customized image segmentation algorithms to identify the positive fluorescence and IHC staining pixels from the tumor region. Specifically, each registered IHC image (5×) was decomposed into a DAB image and a nuclei image with a color deconvolution algorithm (34). Positive NIR fluorescence areas were segmented by first calculating the intensity histogram of the tumor pixels, then fitting the histogram with a "loglogistic" distribution (MATLAB function), and finally experimentally identifying the threshold based on the histogram distribution as previously described (35). Positive EGFR and α-SMA staining areas within the tumor region were segmented through multilevel Otsu's thresholding method (36). The positive ERG staining area was identified with an intensity threshold of 50 through experiment. To identify positive collagen staining, the Masson's Trichrome image was first converted from the RGB color space to L*a*b* color space, k-means clustering algorithm was then used to classify colors in "a*b*" space to identify the blue collagen staining image, and finally a multilevel Otsu's thresholding method was applied to segment collagen positive tumor areas. Binary masks of positive pixels from all these images will be generated for subsequent computing. The last step of the pipeline was to quantify antibody uptake within each tumor as the percent positive NIR fluorescence area fraction per tumor region, and the expression of the molecular markers by computing the percent positive IHC or collagen staining area fraction per tumor area. A composite image can then be generated by super-imposing all the single-marker images followed by pseudo-coloring.

To quantify the architectural complexity of EGFR, vessel, collagen, and α-SMA, we generated binary masks as described above, with the positive objects skeletonized (except for vessel image). Next, the box-counting algorithm (37) was applied on these binary images by starting with single box filling the positive objects of the whole image, progressively reducing the box length ε by a factor of two at each step, and counting the minimum numbers of non-overlapping boxes N(ε) required to cover the positive objects. Fractal dimension (FD) is determined using the following equation:

$$FD = -\lim_{\varepsilon \to 0} \frac{\log N(\varepsilon)}{\log(\varepsilon)}$$

Linear regression using the least-squares method can be performed to obtain the slope of the double logarithmic plot $\log N(\varepsilon)$ versus $\log(\varepsilon)$ with base 10.

To quantify the penetration depth of antibody-dye, the following method was used to plot the fluorescence intensity as a function of distance from the nearest vessel. Two serial images, including the fluorescence image and the vessel image of an adjacent slide, were co-registered and segmented as described above. Then a Euclidian distance map was calculated

from the binary vessel mask. Next, the average background signal from the non-tissue area was subtracted from the raw fluorescence images. Finally, each pixel in the fluorescence image was sorted based on its distance to the nearest vessel, and the fluorescence intensity of panitumumab-IRDye800 was averaged over all pixels at any given distance to the nearest vessel and plotted as a function of distance to the nearest vessel.

Quantitative MRI Data Acquisition and Analysis

Contrast-enhanced T1-weighted MRI scans of the patients prior to surgery were manually segmented by two experienced radiologists specialized in head and neck cancer radiology (Dice score = 0.86). Quantitative imaging features, including first-order statistics (entropy, standard deviation, uniformity, variance) (38) and Haralick texture features (correlation, difference entropy, difference variance, homogeneity, information measure of correlation) (33), were automatically computed from the segmented tumor regions. The correlation coefficients of these features with macroscopic fluorescence image features were calculated. ROC analysis using significant MRI image features were used to classify patients into low or high antibody accumulation or distribution heterogeneity (stratified by the median).

Variable Selection with Univariate and Multivariate Lasso Regression

To identify the most important predictors for antibody delivery, both univariate linear regression and multivariate regression (the least absolute shrinkage and selection operator, or lasso regression) were used. Univariate linear regression analysis was shown with the linear curve fit, and 95% confidence intervals (CI) shaded in gray. Both R^2 (goodness of fit) and P value were shown to indicate the importance of each variable.

Lasso regression is a regularized linear regression algorithm that is among the most effective and efficient methods for feature selection(39). The loss function is defined as follows:

$$\min_{\beta} \sum_{i=1}^{n} \left(y_i - \sum_{j=1}^{p} \beta_j x_{ij} \right)^2 + \lambda \sum_{j=1}^{p} |\beta_j|$$

where y is the response vector; β is the regression coefficient; x is the predictor variable; λ is the tuning parameter that controls the strength of the shrinkage of the variables. Before running the method, variables were normalized with a mean of zero and a standard deviation of one, thereby giving all variables an equal weight in the analysis. The optimal value of λ was determined by five-fold cross-validation (CV) based on the minimum mean squared error (MSE). The optimal λ value was then used for variable selection. The five-fold CV was run for 100 times, and the number of times each variable was selected over the 100 runs were computed to rank the importance of the selected variables. Lasso regression used in this study did not assign a statistical significance (P) value for the selected variables.

All of the above image analysis and regression analysis were conducted with software developed in-house that operates in a MATLAB environment (MATLAB 2018b, MathWorks).

Statistical Methods

Mann-Whitney test was used to compare between two groups, and the Spearman rank-order test or Pearson's correlation test was used for correlation analysis, as appropriate. All statistical tests were two-tailed, and significance was set at a P value less than 0.05. Statistical analyses were performed by the GraphPad Prism software.

Results

Tumor size significantly correlates with intratumoral concentration of panitumumab-IRDye800

Using surgical specimens from HNSCC patients who were infused with panitumumab-IRDye800, we first verified the integrity of the panitumumab-IRDye800CW bioconjugate using the blood and tumor samples from study patients by sodium dodecyl sulfate-polyacrylamide gel electrophoresis (SDS-PAGE). The bioconjugate was not different from the reference standard (152 kDa), nor did we identify the detectable level of antibody-dye fragments or free IRDye800 (Fig. S2), which was consistent with our previous findings nonhuman primates (40), and patient samples after systemic injection of cetuximab-IRDye800 (32). Identification of the intact bioconjugate suggested fluorescence could serve as a surrogate for the localization of the antibody in patient tumor samples.

To understand the impact of tumor biological variables on antibody delivery into HNSCC in the clinical setting, we calculated the Pearson's correlation coefficient between patient clinicopathologic factors and intratumoral concentration of panitumumab-IRDye800 in primary tumors (Table S2). Patient age, sex, and body weight did not correlate with the intratumoral antibody concentration ($P>0.05$). In addition, history of drinking alcohol, smoking, prior chemoradiation, recurrence status, HPV status, and time between infusion and tissue sampling also did not influence intratumoral panitumumab-IRDye800 concentrations ($P>0.05$). Interestingly, tumor size showed a strong and significantly negative correlation (Pearson's $r = -0.60$, $P = 0.0048$). Next, we conducted a multivariate analysis with lasso regression. Tumor size, vessel density, EGFR FD, and dose were the most important determinants selected by lasso regression to predict panitumumab-IRDye800 concentration in fresh patient tumor tissue (Fig. 2A). An inverse correlation was observed between antibody concentration and tumor size (Fig. 2B). To avoid the compounding effect of variations in dose, we normalized the tumor size by antibody dose, and the inverse correlation was still significant (Fig. 2C). More importantly, as tumor size increased, vessel area fraction decreased (Fig. 2D) and EGFR FD increased (Fig. 2E), suggesting that tumor size is the dominant factor predicting intratumoral antibody accumulation. Although several other tumor biological variables including vessel FD, collagen FD, and α-SMA area fraction and FD were also significantly correlated with tumor size (Table S3) and some of these variables showed significant association with intratumoral antibody accumulation in univariate analysis (Table S4), these variables were not selected during the multivariate analysis, suggesting these variables were not as important as vessel area fraction and EGFR FD in predicting antibody delivery.

Tumor growth aggravates the spatial heterogeneity of panitumumab-IRDye800 in both primary and metastatic lesions

Based on microscopic fluorescence imaging of FFPE tissue sections, we analyzed the influence of tumor size on spatial heterogeneity of antibody distribution. Higher spatial heterogeneity was observed in the larger tumors, despite homogenous EGFR expression throughout the tumor (Fig. 3A). We consistently identified higher fluorescence at the periphery compared to the interior of the larger tumors. To quantify the spatial heterogeneity, we calculated the ratio of MFI between the periphery and the interior in representative tissue sections of patients (n = 22) and correlated with tumor size as well as tumor size normalized by dose (Fig. 3B–C), which demonstrated larger differential delivery as tumor size became larger. A comparison of representative regions of interest (ROIs) from the periphery (Fig. 3D) and the interior (Fig. 3E) showed comparable EGFR expression, but higher fluorescence signal, higher vessel area fraction, and lower collagen and α-SMA area fraction in the tumor periphery.

A similar analysis of lymph node metastasis revealed that tumor size was also a significant determinant of antibody delivery into tumor metastasis (Fig. 4). Quantitative analysis revealed a significant inverse relationship between the size of lymph node metastasis and the percent antibody uptake in the metastatic islands of tumor cells (Fig. 4A), and this negative correlation persisted when size was normalized by dose (Fig. 4B). Furthermore, a significant inverse correlation was observed between the vessel area fraction and size of the metastasis (Fig. 4C), while a significant positive relationship was found between EGFR FD and the size of the metastasis (Fig. 4D). A ratio between the fluorescence intensity of the periphery and the interior in representative cross-sections of lymph node metastasis showed a positive correlation with the size of metastasis as well as the size normalized by dose (Fig. 4E–F), suggesting higher spatial heterogeneity of antibody distribution in larger metastasis. Analysis of spatial distribution at the microscopic level was performed on lymph node metastasis of different sizes (Fig. 4G). Three representative examples of lymph node metastasis (ranging from 0.8 mm to 8.5 mm) illustrated homogenous antibody distribution across the smaller metastatic tumor islands (Fig. 4G, first row), but heterogeneous in larger metastatic lesions (Fig. 4G, last two rows), despite relatively even distribution of EGFR expression. Moreover, the distance of antibody extravasation from the nearest vessels was shorter in larger size lymph node metastasis. Consistent with our finding in primary tumors, the antibody was limited to the periphery of the larger metastasis (Fig. 4G) while the interior region had comparatively low fluorescence. This data suggested that tumor size is a significant predictor of the inter-patient and intra-tumoral variations of antibody uptake in both primary tumor and metastatic lesions.

To understand the differential influence of tumor biological variables on antibody delivery into the primary tumor and lymph node metastasis, we calculated antibody delivery as the number of fluorescent pixels normalized for the number of EGFR-positive pixels within the same tumor region, and compared antibody delivery in primary and metastasis. In this analysis, antibody delivery in macrometastatic lesions ((>2mm) was significantly lower than either the primary tumor or micrometastatic lymph nodes (≤ 2mm) (Fig. 5A), although there was no significant difference in EGFR expression of primary and metastasis (Fig. 5B). One

reason for these observations may be a reduction of vessel area fraction in larger metastatic lesions (Fig. 5C). The lower collagen density in micrometastasis than the primary tumor may also contribute to the differential uptake (Fig. 5D), while the density of α-SMA didn't show a significant difference between primary and metastasis (Fig. 5D). This data suggested the differential antibody delivery into primary and metastatic lesions may be attributed to the variations in vessel density and collagen density rather than antigen expression or α-SMA. More importantly, tumor size also plays an important role in the differential uptake of the antibody between primary tumors and lymphatic metastasis.

MRI-derived tumor parameters predict intratumoral concentration and spatial heterogeneity of panitumumab-IRDye800

We hypothesized that contrast-enhanced MRI scan could predict fluorescently labeled antibody delivery into HNSCCs because both MRI contrast agent and fluorescence contrast agent accumulation within the tumors are dependent on the tumor microenvironment. To validate this hypothesis, we developed a quantitative image analysis pipeline (Fig. 6A). Given the strong predictive performance of tumor size for intratumoral antibody concentration, we measured tumor volume from contrast-enhanced T1-weighted MRI. We found significantly higher intratumoral antibody concentration in patients who have smaller tumor volumes (Fig. 6B). More importantly, ROC analysis using the MRI tumor volume showed a sensitivity of 100% and specificity of 87.5% in stratifying patients into low and high antibody uptake (Fig. 6C.).

To assess macroscopic drug distribution, we serially sectioned primary tumor specimens into 5 mm thick tissue sections (Fig. 6D), which then underwent macroscopic fluorescence imaging (Fig. 6E). After imaging, tumor sections were histologically processed into hematoxylin and eosin (H&E) slides and reviewed by a board-certified pathologist to delineate tumor boundaries that were then mapped back to the tissue sections (regions within the black dash line in Fig. 6E) to reconstruct the volumetric tumors. Areas of more intense fluorescence appeared at the periphery suggesting the higher antibody uptake in periphery regions than the interior sections (Fig. 6E). Next, we computed the first-order statistics and the texture features of the fluorescence images of the reconstructed whole-tumor specimen to characterize the uptake and spatial heterogeneity of the antibody to correlate with MRI features. Significantly higher heterogeneity (measured by the inverse of Haralick correlation (33) of the fluorescence intensities in the whole tumor) of antibody distribution was observed in patients with higher heterogeneity (measured by the inverse uniformity of voxel intensities over the volumetric tumor) of MRI contrast distribution in tumors (Fig. 6F), and ROC analysis showed a sensitivity of 88.9% and a specificity of 60% using this MRI metric to classify patients into cohorts of high and low antibody distribution heterogeneity (Fig. 6G). Significant associations were also identified between the entropy and uniformity of MRI tumor intensity with (Haralick) correlation, difference entropy, difference variance, homogeneity, and information measure of correlation of the tumor fluorescence intensity (Fig. S3).

The dose of panitumumab-IRDye800 positively correlates with intratumoral antibody delivery

The concentration of antibody-dye (ng/mg of tissue) was measured in tissue homogenates of the fresh tumor and uninvolved skin and muscle tissue samples (available in 22 patients). Patients receiving 25 mg of panitumumab-IRDye800 had significantly lower tumor drug concentration than those infused with more than 25 mg (Fig. S4 A), indicating that antibody concentration within the tumors arose in a dose-dependent fashion ($P<0.05$), but the concentrations in non-target tissue did not increase significantly ($P>0.05$). A strong positive correlation ($P<0.0005$, Fig. S4 B) was seen between intratumoral antibody concentration results from the NIR plate reader and the MFI of all the tumor sections, indicating that MFI of the tumor volume could be used as a qualitative surrogate of actual antibody concentration. Moreover, the intratumoral antibody accumulation (measured as tumor MFI from fluorescence images of macroscopic sections) in both primary tumor (Fig. S4 C) and lymphatic metastasis (Fig. S4 D) increased with increasing dose, suggesting that macroscopic fluorescence imaging could be a valuable tool to assess dosing schedules. Finally, we compared primary tumor and metastatic lymph nodes at the macroscopic level, using tumor MFI in the low dose (25mg) and high dose cohort (>25mg) and found significantly higher antibody uptake in the primary tumor compared to the metastasis in both dosing cohorts (Fig. S4 E).

Discussion

The efficacy of targeted therapy with antibodies depends on successful drug delivery into the tumor, therefore there is a critical clinical need to measure intratumoral antibody uptake and distribution to guide dose optimization and patient selection. Although preclinical studies have observed heterogeneous antibody delivery into solid tumors and suggested the impact of many tumor biological variables on drug delivery, there is limited clinical data to confirm these reports and hypotheses in human tumors. The large gap between preclinical efficacy and clinical outcomes necessitates direct measurement and prediction of drug delivery in human patients. To bridge the knowledge gap, we developed a clinically applicable imaging and computational platform and presented the first-in-human clinical data that evaluated the feasibility of this platform to measure and predict antibody delivery into human HNSCC. To the best of our knowledge, this work is the first of its kind to demonstrate the feasibility of using contrast-enhanced MRI to predict intratumoral antibody delivery into patients. This study suggested that fluorescently labeled therapeutic antibodies could be used as a valuable tool in the clinic to validate the preclinical hypotheses about drug delivery and to evaluate potential strategies to increase the distribution of antibodies and other macromolecular drugs in solid tumors. Furthermore, this study may have implications for dose optimization and response prediction in antibody-based therapeutics across multiple tumor types in early phase clinical trials.

Using surgical specimens from patients who were systemically infused with fluorescently labeled therapeutic antibody, this study not only confirmed heterogeneous intratumoral antibody distribution in line with many preclinical reports (14,15,17,24), but also quantified the extent of inter-patient, inter-tumor, and intra-tumor heterogeneity of antibody delivery in

patients. Overall, larger tumors have more heterogeneous antibody distribution than smaller tumors, and primary tumors have significantly more heterogeneous antibody distribution than lymph node metastasis. While macrometastasis in the lymph nodes suffered from non-uniform antibody distribution, micrometastasis and smaller tumors seemed to have a more uniform distribution. We showed that this differential antibody delivery was related to the differences in vessel and collagen area fraction but not target expression levels, which supported the previous hypothesis that small tumors were prevascularized with shorter diffusion distances and less stromal barriers (7). In addition, despite homogenous antigen expression across the tumor, up to three-fold differences were observed between antibody accumulation in the periphery and interior of the primary tumor and lymph node metastasis. Interestingly, this concentration gradient was not as dramatic as predicted by preclinical models (41,42). At the microscopic level, heterogeneous antibody distribution was observed in isolated tumor nests or islands, with perivascular antibody distribution in larger tumor nests but full antibody penetration into smaller tumor nests. This data provided the first microscopic clinical data to directly confirm the binding-site barrier that was proposed by Weinstein and colleagues (22,43,44), which described that antibody penetration into solid tumors could be prevented by the very fact of their successful binding to the target antigen. Collectively, this study represented the first-in-human imaging and quantification of the antibody distribution heterogeneity in human HNSCC at both macroscopic and microscopic levels, which can motivate cancer researchers to develop new strategies to increase the homogeneity of intratumoral antibody distribution and also provide a clinically applicable platform to evaluate these strategies.

A further novel finding is the strong predictive value of tumor size for intratumoral antibody accumulation and spatial distribution in both primary tumor and lymph node metastasis. Building on previous reports about the impact of various tumor biological parameters on antibody delivery into solid tumors (12,14,20–22,32,41), this study used a machine learning algorithm (LASSO regression) to rank the relative predictive value of representative tumor biological variables. Among tumor size, and the positive area fraction and fractal dimension of the vessel, target antigen (EGFR), collagen, and α-SMA, this study identified tumor size as the most important variable to predict the intratumoral accumulation into HNSCC. Although vessel area fraction and EGFR fractal dimension were also identified as important predictors, both metrics showed significant correlation with tumor size. Other variables that significantly correlate with tumor size include vessel FD and collagen FD in both primary and metastasis, but these two variables were not predictive of intratumoral antibody concentration, suggesting not all the tumor biological parameters are equally important. Furthermore, the spatial heterogeneity of antibody distribution also increased as tumor size increased in both primary and metastasis, as evidenced by the larger differences in antibody accumulation between the periphery and interior of tumors. These findings suggest that as tumors grow larger, tumor microenvironment factors evolve accordingly to create more pathophysiological barriers, leading to low and heterogeneous antibody delivery into larger tumors. This is in accordance with the preclinical hypothesis that the interstitial pressure and solid stress increase as tumors grow larger, which prevent the antibody from penetrating deeper into larger tumors (41,42). Most importantly, we showed the feasibility of using tumor volumes measured by the standard-of-care MRI to stratify patients into groups of

low and high intratumoral antibody accumulation with good sensitivity and specificity, suggesting the strong translational potential of this finding. This finding has significant implications in the identification of patients most likely to have improved drug penetration (thereby identifying patients for treatment or reduced dose) in early phase clinical trials.

To facilitate clinical translation of the proposed platform, we showed the feasibility of using clinically available MRI to predict intratumoral antibody accumulation and distribution, which could be used to select patients most likely to respond to antibody-based therapeutics. The rationale for using noninvasive clinical imaging as a diagnostic companion to predict patient response can be from two different perspectives. The first one is to select patients with high intratumoral drug accumulation based on the enhanced permeability and retention (EPR) effect. Recently, MRI imaging of ferumoxytol nanoparticle in tumor lesions has been correlated with lesion shrinkage in response to nanoliposomal irinotecan (6). In another study, positron emission tomography (PET) imaging of nanoparticle deposition in tumors has been shown to correlate with favorable patient response to trastuzumab (45). These studies suggested that noninvasive clinical imaging of contrast agents can be predictive of patient response to systemic therapy. Another rationale involves the use of artificial intelligence to infer the correlation between radiomic imaging features and patient responses. Two recent studies reported the feasibility of using radiomics signature from pre-treatment contrast-enhanced CT to predict patient response to immunotherapy using checkpoint inhibitors (monoclonal antibodies) (46,47). Our study utilized the strong predictive value of tumor size to predict intratumoral antibody accumulation. Moreover, we extracted imaging features describing contrast distribution within the tumor to correlate with fluorescently labeled antibody distribution in the same tumor. The integration of pre-treatment contrast-enhanced MRI with fluorescence measurement is highly novel with significant implications in dose optimization and patient selection in early phase clinical trials.

To achieve sufficiently high and homogenous antibody distribution in solid tumors, it is critically important to determine the optimal dose for individual patients. It has been increasingly recognized that the measurement of antibody penetration into solid tumors is an important but missing piece of information towards personalized dosing (5,8,48). Conventional dosing strategy based on the maximum tolerated dose (MTD) is generally considered inappropriate for targeted agents since dose-response relationships more closely relate to adequate target occupancy and inhibition rather than toxicities (49). During early-phase clinical trials, dose optimization for therapeutic antibodies can be difficult since therapeutic efficacy and toxicity can vary across patients. Current pharmacokinetic studies of anticancer drugs rely on plasma drug concentration as a surrogate for tumor drug level, but blood pharmacokinetics is a poor indicator of tumor phamacokinetics. The concentration of panitumumab-IRDye800 measured in tumors, when delivered in a sub-therapeutic range, did not correlate with traditional dosing parameters such as patient body weight ($P < 0.05$). Instead, we identified the tumor size to be a key determinant for reduced antibody delivery and increased spatial homogeneity in both primary tumors and regional nodal metastasis. This is consistent with recent data challenging the strategy of dosing monoclonal antibodies by patient body weight based on years of data on toxicity and efficacy (50). Because we have shown that the antibody is minimally altered by the addition of the dye (40), this

molecular imaging approach may allow the study of other antibody-based therapeutics in clinical trials.

In summary, we developed a clinical applicable platform to measure and predict antibody delivery into HNSCC that can be broadly applicable and valuable to studying macromolecular drugs including therapeutic antibodies, antibody-drug conjugates, immune check-point inhibitors, nanomedicines, etc. in multiple cancer types in the clinic, especially those that are difficult to model in animal models such as desmoplastic microenvironment and metastatic lesions. The proposed clinical workflow may enable us to identify the right patients and the right dose in early-phase clinical trials.

Supplementary Material

Refer to Web version on PubMed Central for supplementary material.

Acknowledgments:

We acknowledge the support of NIH R01 CA190306–01 (E.L.R), the Stanford Molecular Imaging Scholars (SMIS) program (NIH T32CA118681, G.L.), the Netherlands Organization for Scientific Research (Rubicon; 019.171LW.022, N.S.V.), and the Stanford University School of Medicine Medical Scholars Program (S.F.). We thank the surgery teams in the department of Otolaryngology for tissue collection, Shirley Kwok for tissue sectioning, and Kristen M. Cunanan for her statistical consulting.

Financial support: This work was supported by NIH R01 CA190306–01 (E.L.R), the Stanford Molecular Imaging Scholars (SMIS) program (NIH T32 CA118681, G.L.), the Netherlands Organization for Scientific Research (Rubicon; 019.171LW.022, N.S.V.), and the Stanford University School of Medicine Medical Scholars Program (S.F.).

References

1. Carter P Improving the efficacy of antibody-based cancer therapies. Nature Reviews Cancer 2001;1:118 doi 10.1038/35101072. [PubMed: 11905803]
2. Weiner LM, Surana R, Wang S. Monoclonal antibodies: versatile platforms for cancer immunotherapy. Nature Reviews Immunology 2010;10:317 doi 10.1038/nri2744.
3. Kleppe M, Levine RL. Tumor heterogeneity confounds and illuminates: assessing the implications. Nature Medicine 2014;20:342 doi 10.1038/nm.3522.
4. Minchinton AI, Tannock IF. Drug penetration in solid tumours. Nature Reviews Cancer 2006;6:583 doi 10.1038/nrc1893. [PubMed: 16862189]
5. Bartelink IH, Jones EF, Shahidi-Latham SK, Lee PRE, Zheng Y, Vicini P, et al. Tumor drug penetration measurements could be the neglected piece of the personalized cancer treatment puzzle. Clinical Pharmacology & Therapeutics 2018;0(0) doi doi:10.1002/cpt.1211.
6. Ramanathan RK, Korn RL, Raghunand N, Sachdev JC, Newbold RG, Jameson G, et al. Correlation between Ferumoxytol Uptake in Tumor Lesions by MRI and Response to Nanoliposomal Irinotecan in Patients with Advanced Solid Tumors: A Pilot Study. Clinical Cancer Research 2017;23(14):3638–48 doi 10.1158/1078-0432.ccr-16-1990. [PubMed: 28159813]
7. Garattini S, Fuso Nerini I, D'Incalci M. Not only tumor but also therapy heterogeneity. Annals of Oncology 2018;29(1):13–9 doi 10.1093/annonc/mdx646. [PubMed: 29045538]
8. Ruiz-Cerdá L, Asin-Prieto E, Parra-Guillen ZP, Troconiz IF. The long neglected player: modeling tumor uptake to guide optimal dosing. Clinical Cancer Research 2018:clincanres.0580.2018 doi 10.1158/1078-0432.ccr-18-0580.
9. Adjei AA. What is the right dose? The elusive optimal biologic dose in phase I clinical trials. Journal of Clinical Oncology 2006;24(25):4054–5 doi 10.1200/jco.2006.07.4658. [PubMed: 16943522]

10. Keizer RJ, Huitema AD, Schellens JH, Beijnen JH. Clinical pharmacokinetics of therapeutic monoclonal antibodies. Clinical pharmacokinetics 2010;49(8):493–507 doi 10.2165/11531280-000000000-00000. [PubMed: 20608753]
11. Trédan O, Galmarini CM, Patel K, Tannock IF. Drug resistance and the solid tumor microenvironment. JNCI: Journal of the National Cancer Institute 2007;99(19):1441–54 doi 10.1093/jnci/djm135. [PubMed: 17895480]
12. Thurber GM, Schmidt MM, Wittrup KD. Factors determining antibody distribution in tumors. Trends in Pharmacological Sciences 2008;29(2):57–61 doi 10.1016/j.tips.2007.11.004. [PubMed: 18179828]
13. Sriraman SK, Aryasomayajula B, Torchilin VP. Barriers to drug delivery in solid tumors. Tissue Barriers 2014;2:e29528 doi 10.4161/tisb.29528.
14. Baker JHE, Lindquist KE, Huxham LA, Kyle AH, Sy JT, Minchinton AI. Direct Visualization of Heterogeneous Extravascular Distribution of Trastuzumab in Human Epidermal Growth Factor Receptor Type 2 Overexpressing Xenografts. Clinical Cancer Research 2008;14(7):2171–9 doi 10.1158/1078-0432.ccr-07-4465. [PubMed: 18381959]
15. Lee CM, Tannock IF. The distribution of the therapeutic monoclonal antibodies cetuximab and trastuzumab within solid tumors. BMC Cancer 2010;10(1):255 doi 10.1186/1471-2407-10-255. [PubMed: 20525277]
16. Freeman DJ, McDorman K, Ogbagabriel S, Kozlosky C, Yang B-B, Doshi S, et al. Tumor penetration and epidermal growth factor receptor saturation by panitumumab correlate with antitumor activity in a preclinical model of human cancer. 2012;11(1):47 doi 10.1186/1476-4598-11-47.
17. Baker JHE, Kyle AH, Reinsberg SA, Moosvi F, Patrick HM, Cran J, et al. Heterogeneous distribution of trastuzumab in HER2-positive xenografts and metastases: role of the tumor microenvironment. Clinical & Experimental Metastasis 2018;35(7):691–705 doi 10.1007/s10585-018-9929-3. [PubMed: 30196384]
18. Schweitzer AD, Rakesh V, Revskaya E, Datta A, Casadevall A, Dadachova E. Computational model predicts effective delivery of 188-Re-labeled melanin-binding antibody to metastatic melanoma tumors with wide range of melanin concentrations. Melanoma research 2007;17(5):291–303 doi 10.1097/CMR.0b013e3282eeeae7. [PubMed: 17885584]
19. Stylianopoulos T, Jain RK. Combining two strategies to improve perfusion and drug delivery in solid tumors. Proceedings of the National Academy of Sciences 2013;110(46):18632–7 doi 10.1073/pnas.1318415110.
20. Netti PA, Berk DA, Swartz MA, Grodzinsky AJ, Jain RK. Role of Extracellular Matrix Assembly in Interstitial Transport in Solid Tumors. Cancer Research 2000;60(9):2497–503. [PubMed: 10811131]
21. Stylianopoulos T, Martin JD, Chauhan VP, Jain SR, Diop-Frimpong B, Bardeesy N, et al. Causes, consequences, and remedies for growth-induced solid stress in murine and human tumors. Proceedings of the National Academy of Sciences 2012;109(38):15101–8 doi 10.1073/pnas.1213353109.
22. Weinstein JN, van Osdol W. Early intervention in cancer using monoclonal antibodies and other biological ligands: micropharmacology and the “binding site barrier”. Cancer Res 1992;52(9 Suppl):2747s-51s.
23. Thurber GM, Weissleder R. Quantitating Antibody Uptake In Vivo: Conditional Dependence on Antigen Expression Levels. Molecular Imaging and Biology 2011;13(4):623–32 doi 10.1007/s11307-010-0397-7. [PubMed: 20809210]
24. Rhoden JJ, Wittrup KD. Dose dependence of intratumoral perivascular distribution of monoclonal antibodies. Journal of pharmaceutical sciences 2012;101(2):860–7 doi 10.1002/jps.22801. [PubMed: 22057714]
25. Gould SE, Junttila MR, de Sauvage FJ. Translational value of mouse models in oncology drug development. Nature Medicine 2015;21:431 doi 10.1038/nm.3853.
26. Junttila MR, de Sauvage FJ. Influence of tumour micro-environment heterogeneity on therapeutic response. Nature 2013;501:346 doi 10.1038/nature12626. [PubMed: 24048067]

27. Lamberts LE, Williams SP, Scheltinga AGTTv, Hooge MNL-d, Schröder CP, Gietema JA, et al. Antibody Positron Emission Tomography Imaging in Anticancer Drug Development. Journal of Clinical Oncology 2015;33(13):1491–504 doi 10.1200/jco.2014.57.8278. [PubMed: 25779566]
28. Lindenberg L, Adler S, Turkbey IB, Mertan F, Ton A, Do K, et al. Dosimetry and first human experience with (89)Zr-panitumumab. Am J Nucl Med Mol Imaging 2017;7(4):195–203. [PubMed: 28913158]
29. Bensch F, Smeenk MM, van Es SC, de Jong JR, Schroder CP, Oosting SF, et al. Comparative biodistribution analysis across four different (89)Zr-monoclonal antibody tracers-The first step towards an imaging warehouse. Theranostics 2018;8(16):4295–304 doi 10.7150/thno.26370. [PubMed: 30214621]
30. Niu G, Li Z, Xie J, Le Q-T, Chen X. PET of EGFR Antibody Distribution in Head and Neck Squamous Cell Carcinoma Models. Journal of Nuclear Medicine 2009;50(7):1116–23 doi 10.2967/jnumed.109.061820. [PubMed: 19525473]
31. Gao RW, Teraphongphom NT, van den Berg NS, Martin BA, Oberhelman NJ, Divi V, et al. Determination of Tumor Margins with Surgical Specimen Mapping Using Near-Infrared Fluorescence. Cancer Research 2018;78(17):5144–54 doi 10.1158/0008-5472.can-18-0878. [PubMed: 29967260]
32. de Boer E, Warram JM, Tucker MD, Hartman YE, Moore LS, de Jong JS, et al. In vivo fluorescence immunohistochemistry: localization of fluorescently labeled cetuximab in squamous cell carcinomas. Scientific Reports 2015;5:10169 doi 10.1038/srep10169.
33. Haralick RM, Shanmugam K, Dinstein I. Textural Features for Image Classification. IEEE Transactions on Systems, Man, and Cybernetics 1973;SMC-3(6):610–21 doi 10.1109/TSMC.1973.4309314.
34. Ruifrok AC, Johnston DA. Quantification of histochemical staining by color deconvolution. Analytical and quantitative cytology and histology 2001;23(4):291–9. [PubMed: 11531144]
35. Lu G, Little JV, Wang X, Zhang H, Patel MR, Griffith CC, et al. Detection of head and neck cancer in surgical specimens using quantitative hyperspectral imaging. Clinical Cancer Research 2017 doi 10.1158/1078-0432.ccr-17-0906.
36. Otsu N A threshold selection method from gray-level histograms. IEEE Transactions on Systems, Man, and Cybernetics 1979;9(1):62–6 doi 10.1109/TSMC.1979.4310076.
37. Chen C, He Z-c, Shi Y, Zhou W, Zhang X, Xiao H-l, et al. Microvascular fractal dimension predicts prognosis and response to chemotherapy in glioblastoma: an automatic image analysis study. Laboratory Investigation 2018;98(7):924–34 doi 10.1038/s41374-018-0055-2. [PubMed: 29765109]
38. Aerts HJWL, Velazquez ER, Leijenaar RTH, Parmar C, Grossmann P, Carvalho S, et al. Decoding tumour phenotype by noninvasive imaging using a quantitative radiomics approach. Nature Communications 2014;5(1):4006 doi 10.1038/ncomms5006.
39. Jamshidi A, Pelletier J-P, Martel-Pelletier J. Machine-learning-based patient-specific prediction models for knee osteoarthritis. Nature Reviews Rheumatology 2019;15(1):49–60 doi 10.1038/s41584-018-0130-5. [PubMed: 30523334]
40. Zinn KR, Korb M, Samuel S, Warram JM, Dion D, Killingsworth C, et al. IND-directed safety and biodistribution study of intravenously injected cetuximab-IRDye800 in cynomolgus macaques. Molecular imaging and biology : MIB : the official publication of the Academy of Molecular Imaging 2015;17(1):49–57 doi 10.1007/s11307-014-0773-9.
41. Jain RK. Physiological barriers to delivery of monoclonal antibodies and other macromolecules in tumors. Cancer Research 1990;50(3 Supplement):814s–9s. [PubMed: 2404582]
42. Stylianopoulos T, Martin JD, Snuderl M, Mpekris F, Jain SR, Jain RK. Coevolution of Solid Stress and Interstitial Fluid Pressure in Tumors During Progression: Implications for Vascular Collapse. Cancer Research 2013;73(13):3833–41 doi 10.1158/0008-5472.can-124521. [PubMed: 23633490]
43. Juweid M, Neumann R, Paik C, Perez-Bacete MJ, Sato J, van Osdol W, et al. Micropharmacology of Monoclonal Antibodies in Solid Tumors: Direct Experimental Evidence for a Binding Site Barrier. Cancer Research 1992;52(19):5144–53. [PubMed: 1327501]
44. Saga T, Neumann RD, Heya T, Sato J, Kinuya S, Le N, et al. Targeting cancer micrometastases with monoclonal antibodies: a binding-site barrier. Proceedings of the National Academy of

Sciences of the United States of America 1995;92(19):8999–9003 doi 10.1073/pnas.92.19.8999. [PubMed: 7568060]

45. Lee H, Shields AF, Siegel BA, Miller KD, Krop I, Ma CX, et al. 64Cu-MM-302 Positron Emission Tomography Quantifies Variability of Enhanced Permeability and Retention of Nanoparticles in Relation to Treatment Response in Patients with Metastatic Breast Cancer. Clinical Cancer Research 2017;23(15):4190–202 doi 10.1158/1078-0432.ccr-16-3193. [PubMed: 28298546]
46. Sun R, Limkin EJ, Vakalopoulou M, Dercle L, Champiat S, Han SR, et al. A radiomics approach to assess tumour-infiltrating CD8 cells and response to anti-PD-1 or anti-PD-L1 immunotherapy: an imaging biomarker, retrospective multicohort study. The Lancet Oncology 2018;19(9):1180–91 doi 10.1016/S1470-2045(18)30413-3. [PubMed: 30120041]
47. Trebeschi S, Drago SG, Birkbak NJ, Kurilova I, Calin AM, Pizzi AD, et al. Predicting Response to Cancer Immunotherapy using Non-invasive Radiomic Biomarkers. Annals of oncology : official journal of the European Society for Medical Oncology 2019 doi 10.1093/annonc/mdz108.
48. Ribba B, Boetsch C, Nayak T, Grimm HP, Charo J, Evers S, et al. Prediction of the Optimal Dosing Regimen Using a Mathematical Model of Tumor Uptake for Immunocytokine-Based Cancer Immunotherapy. Clinical Cancer Research 2018;24(14):3325–33 doi 10.1158/1078-0432.ccr-17-2953. [PubMed: 29463551]
49. Sachs JR, Mayawala K, Gadamsetty S, Kang SP, de Alwis DP. Optimal dosing for targeted therapies in oncology: drug development cases leading by example. Clinical Cancer Research 2016;22(6):1318–24 doi 10.1158/1078-0432.ccr-15-1295. [PubMed: 26597302]
50. Hendrikx JJMA, Haanen JBAG, Voest EE, Schellens JHM, Huitema ADR, Beijnen JH. Fixed dosing of monoclonal antibodies in oncology. The Oncologist 2017;22(10):1212–21 doi 10.1634/theoncologist.2017-0167. [PubMed: 28754722]

Translational relevance:

This study developed and validated a clinically translatable imaging and computation platform to quantify and predict antibody delivery in head and neck cancers in a clinical study. We uncovered significant inter-patient, inter-tumor, and intra-tumor heterogeneity of antibody distribution, and identified tumor size as a key predictor for intratumoral antibody accumulation, which has significant implications for dose optimization and response prediction in antibody-based therapeutics. This study casts new light on the understanding of clinically relevant antibody distribution in human solid tumors. The proposed platform can be used to bridge the gap between preclinical hypothesis and clinical findings and to assess new strategies to improve antibody dosing and delivery into solid tumors in early phase clinical trials.

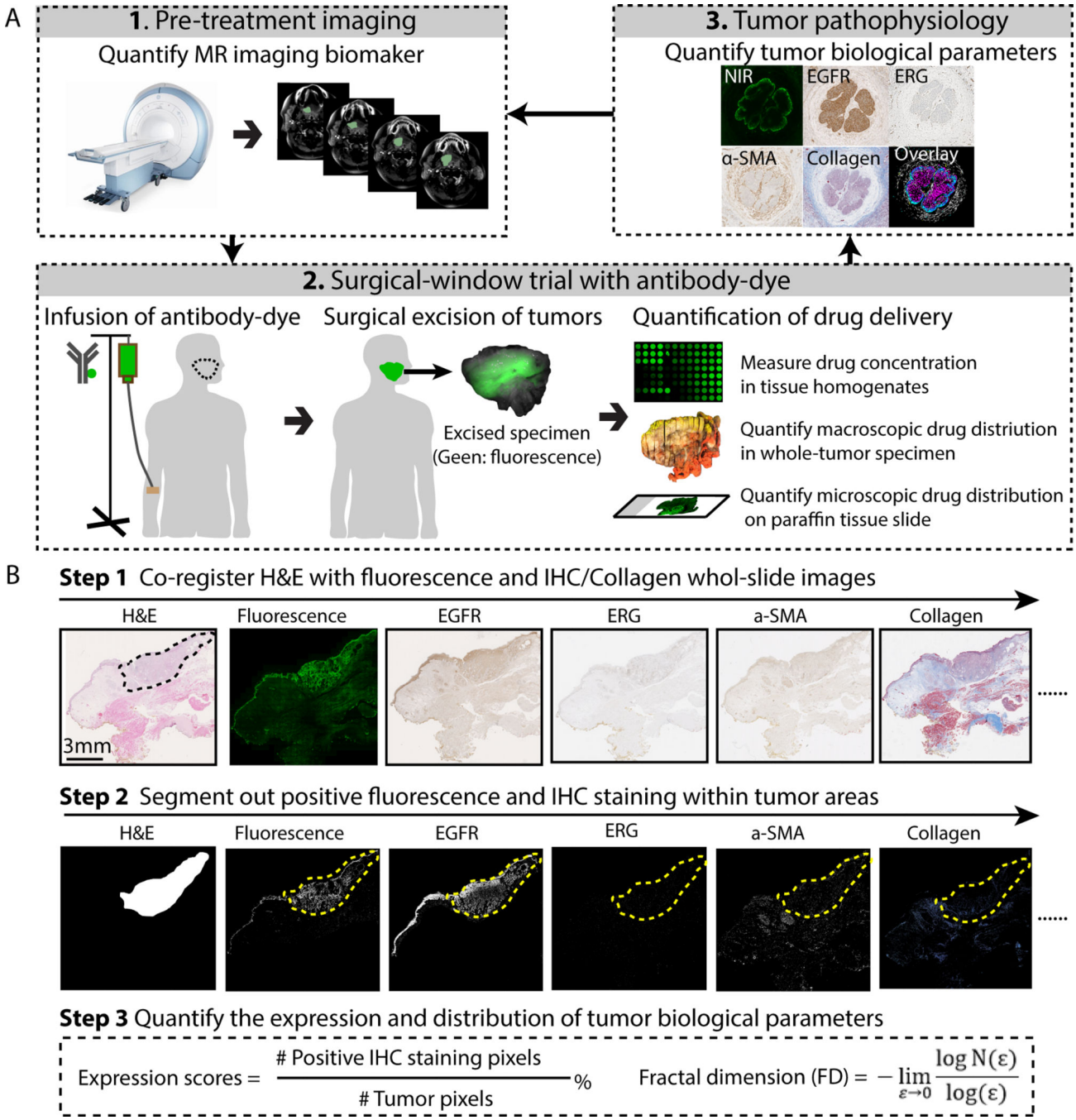

Fig. 1.

Overview of the clinical study design. (**A**) This study involved three major components: firstly, patients received contrast-enhanced T1-weighted MRI scans and imaging features were computed from the MRI data to correlate with antibody delivery. Secondly, patients were enrolled into a surgical-window trial during which they were systemically administered with panitumumab-IRDye800 and then underwent surgical tumor resection. The intratumoral antibody concentration was measured from tumor homogenates as ng/mg of tumor tissue. The macroscopic drug distribution was quantified from the reconstructed

whole-tumor specimen. The microscopic drug distribution was quantified on FFPE tissue slides. Finally, tumor biological parameters were measured from multiple IHC staining of serial tumor sections to correlate with microscopic antibody distribution. (**B**) The proposed quantitative image analysis pipeline was used to derive metrics for measuring tumor biological parameters. This pipeline involved co-registration and segmentation of the whole-slide digital pathology images of multiple tumor markers, including immunohistochemistry (IHC) staining of EGFR, ERG (vessel), α-smooth muscle actin (α-SMA), and collagen (Masson's trichrome stain), etc. Positive staining area fraction and fractal dimension were computed from the segmented tumor areas of these images to represent the density and the architectural complexity of individual markers.

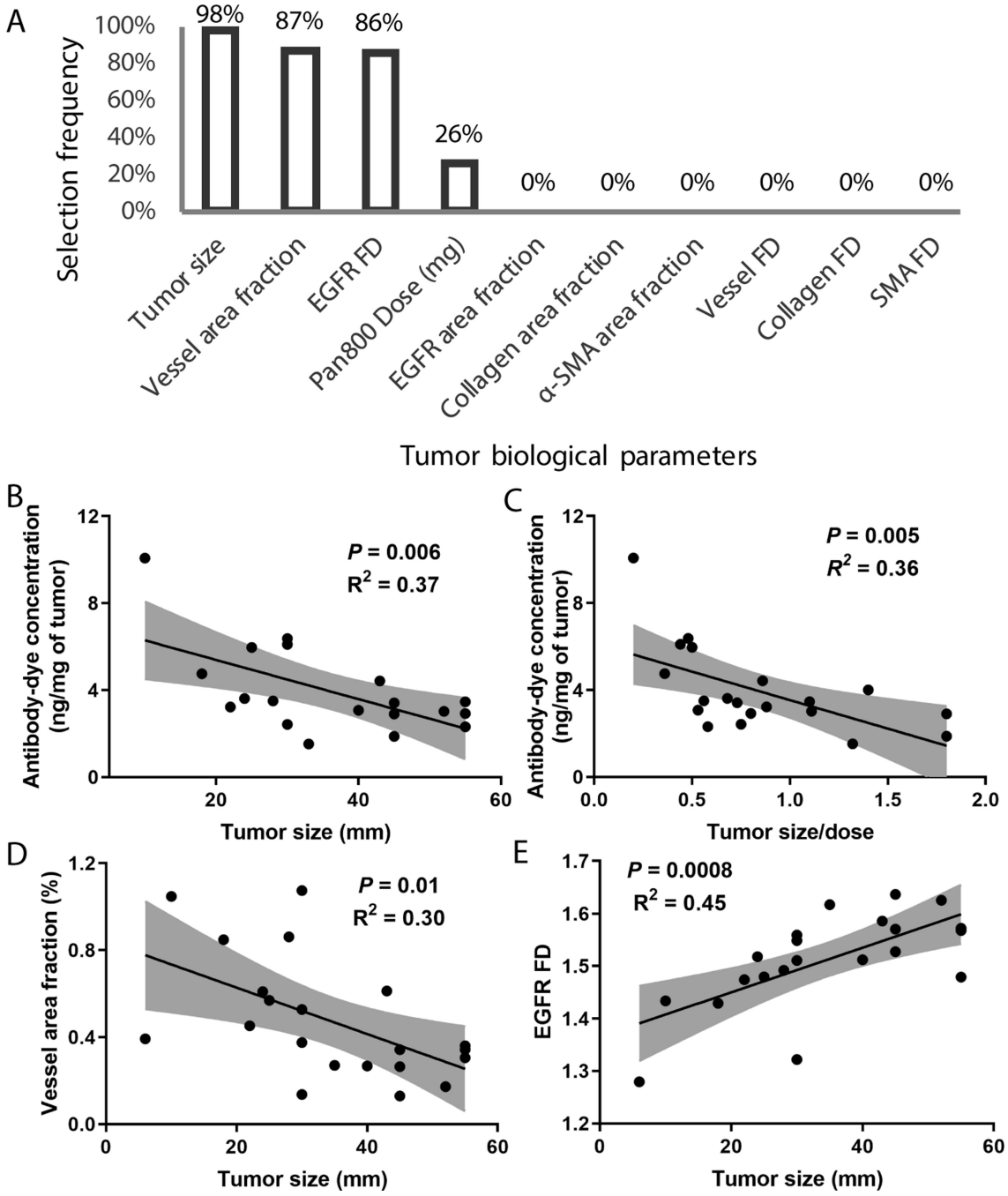

Fig. 2.

Tumor size was identified as the most important predictor for intratumoral antibody accumulation. (**A**) Tumor size, vessel density, EGFR FD, and dose were the most important determinants of antibody concentration in tumor tissue as selected by lasso regression. (**B-C**) Intratumoral antibody concentration of individual patients was negatively correlated with tumor size. (**D-E**) Both vessel area fraction and EGFR FD were significantly correlated with tumor size.

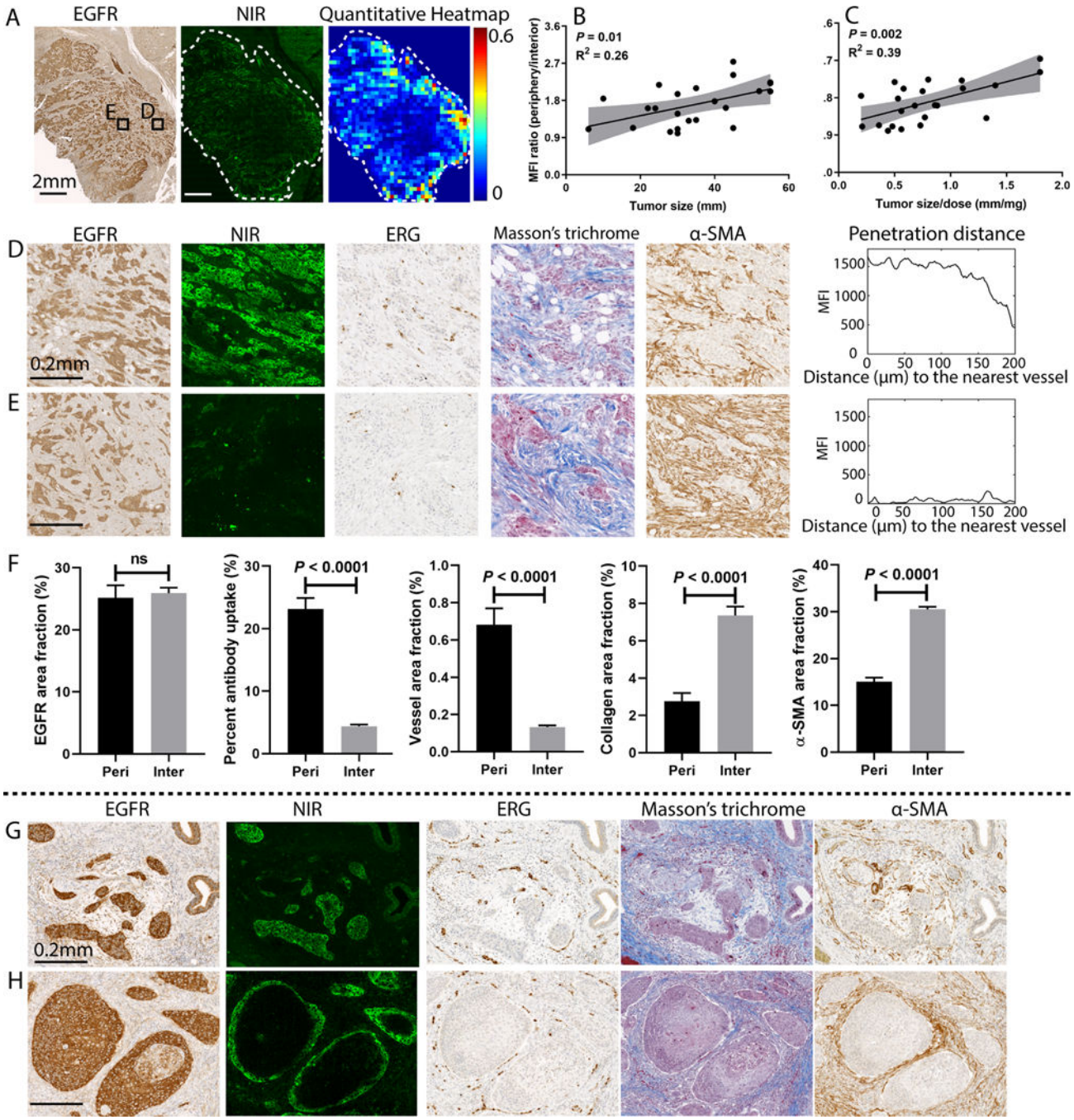

Fig. 3.

The microscopic spatial heterogeneity of antibody distribution within primary tumors was dependent on tumor size. (**A**) A representative example showed higher antibody accumulation in the tumor periphery than the interior despite consistent EGFR expressions across the tumor. (**B-C**) The ratio of the mean fluorescence intensity between the periphery and interior of tumors increased with larger tumor size. (**D-F**) Comparison of selected regions (ROI D&E) of the tumor in panel (**A**) demonstrated comparable EGFR expression, higher antibody uptake, higher vessel area fraction, lower collagen area fraction, and lower

α-SMA area fraction in the periphery than the interior tumor area. When antibody delivery (measured in MFI) was plotted against the distance from the nearest blood vessel, the periphery had much higher fluorescence signal, while the interior had minimal fluorescence signal. (**G**-**H**) Despite homogeneous EGFR expression, antibody only penetrated a few cell layers in larger tumor nests while fully penetrated smaller tumor nests, and antibody distribution showed peri-vascular pattern. (Mann-Whitney test, error bar means standard error).

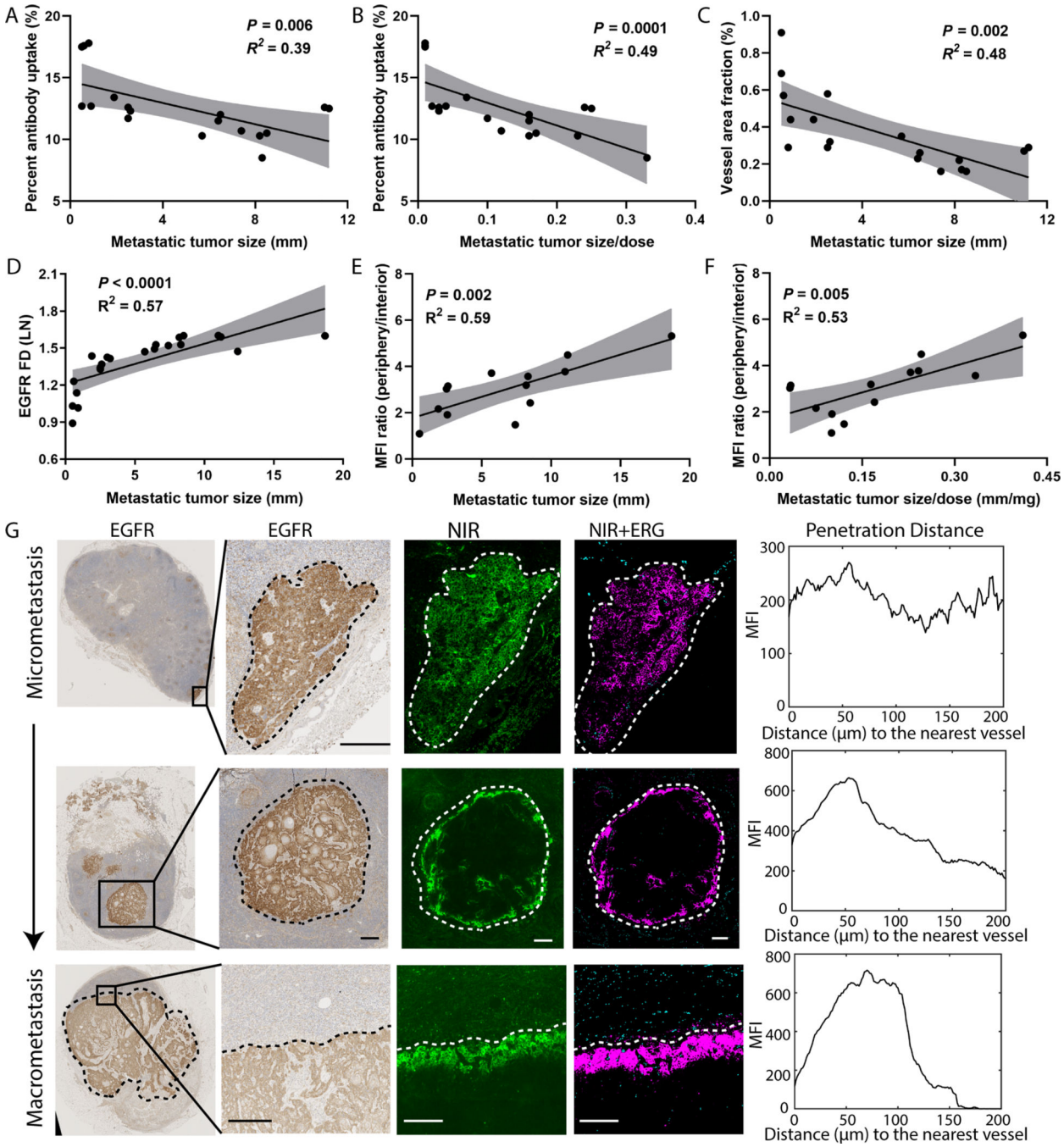

Fig. 4.

Microscopic heterogeneity of antibody distribution in metastatic lymph nodes was dependent on the size of metastasis. (**A-B**) Antibody delivery negatively correlated with metastatic tumor size, even when normalized for dose. (**C-D**) Consistent with the findings in primary tumors, increased tumor size correlated with a reduced vessel area fraction and increased EGFR FD. (**E-F**) The ratio of the mean fluorescence intensity between periphery and interior of metastatic lesions significantly increased with tumor size. (**G**) Spatial heterogeneity of antibody distribution within lymph node metastasis increased as metastatic

tumor size increased despite homogenous EGFR expression. The plots of fluorescence intensity as a function of distance to the nearest vessels for the selected ROIs showed reduced penetration distance in larger metastasis. (Scale bar: 200 μm).

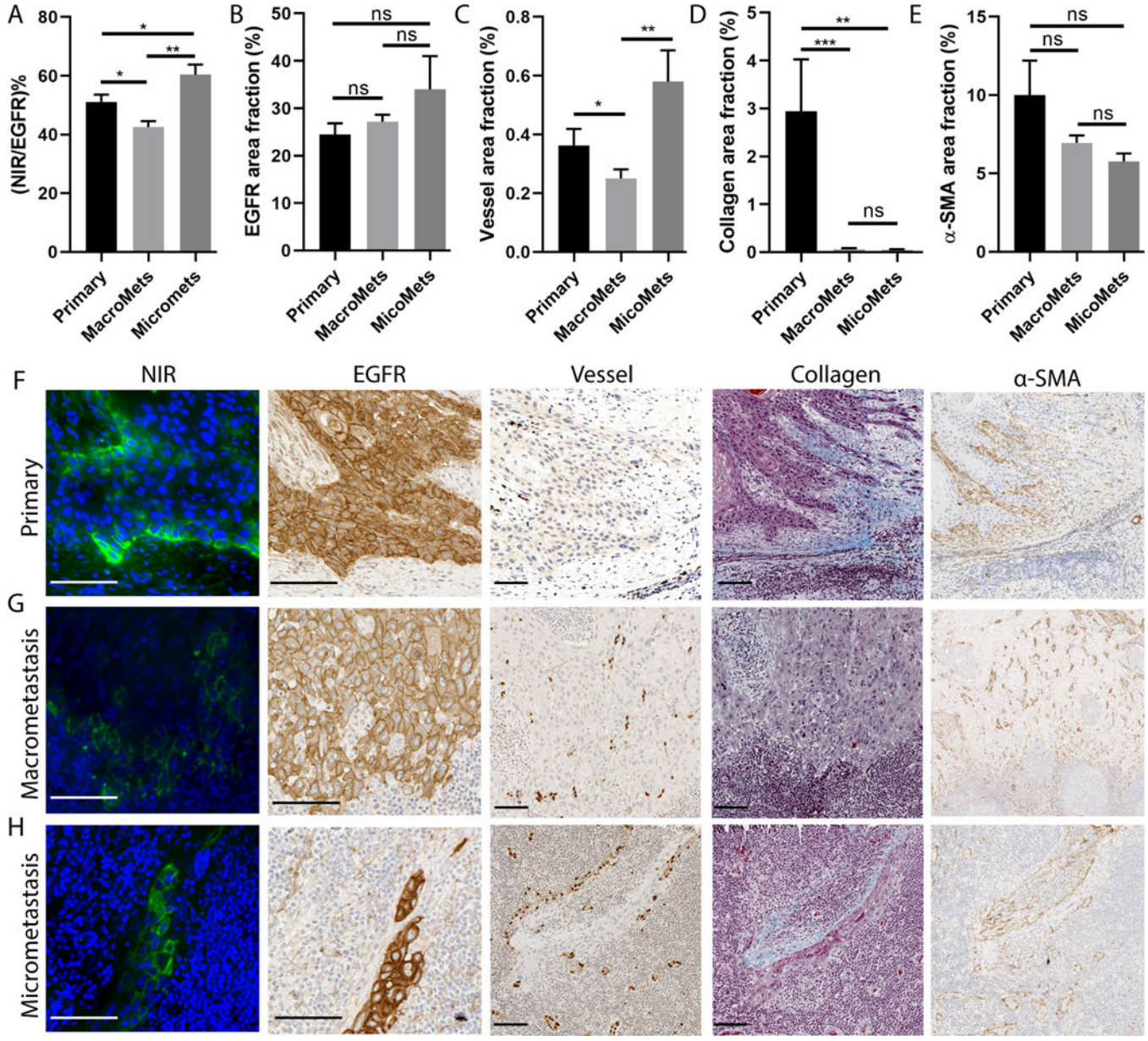

Fig. 5.

Comparison between primary tumor and lymph node metastasis showed their differential uptake was related to tumor size. (**A**) The ratio of positive NIR fluorescence area normalized by EGFR positive tumor area for the micrometastasis and primary tumors were significantly higher than that in the macrometastasis. (**B**) The EGFR expression showed no significant difference between the primary and metastasis. (**C**) The vessel area fraction for micrometastasis and primary tumors were significantly higher than that in macrometastasis. (**D**) Collagen area fraction was significantly higher in primary tumor than that in metastasis. (**E**) α-SMA area fraction showed no difference between primary and metastasis. (ns: P>0.05, **P*<0.05, ***P*<0.01, ****P*<0.001, Mann-Whitney test, error bar means standard error). (**F-H**) Representative images of the primary tumor, macrometasis,

and micrometastasis from the same patient showed heterogeneous NIR fluorescence microscopic image (green: NIR, blue: DAPI nuclei) despite homogenous EGFR expression, which may be due to the differential expression of vessel and collagen in these tumor regions. (Scale bar: 100 μm)

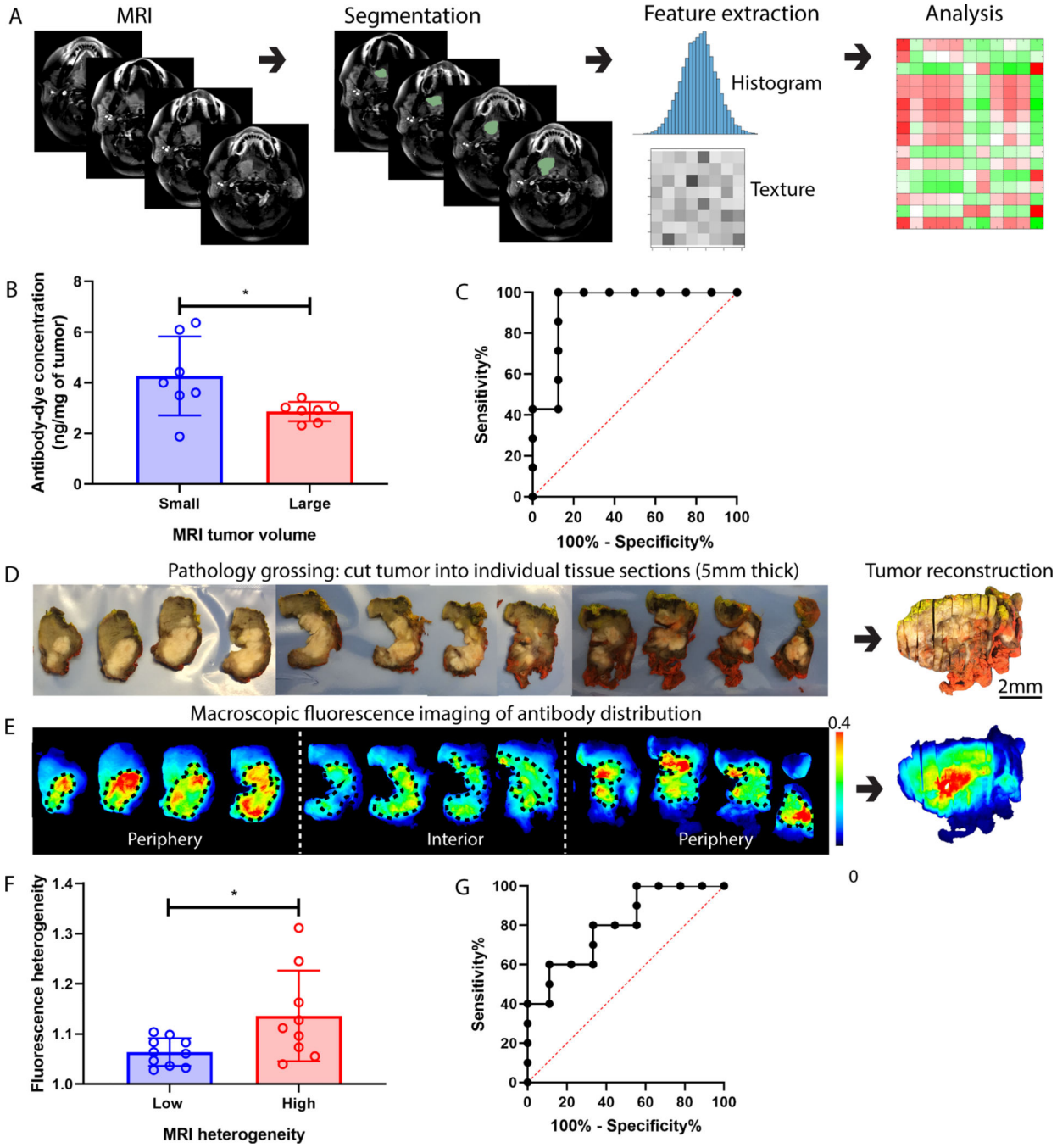

Fig. 6.

MRI can predict antibody delivery into patient HNSCC. (**A**) The MRI image analysis pipeline included tumor segmentation, feature extraction, and correlation analysis with antibody delivery. (**B**) Intratumoral antibody concentration was significantly higher in patients with smaller MRI tumor volume. (**C**) ROC analysis showed that MRI tumor volume can predict intratumoral antibody concentration with good sensitivity and specificity. (**D-E**) showed the standard-of-care pathological grossing procedure involving cutting the primary specimen into individual 5-mm thick tissue sections which were imaged with a

macroscopic fluorescence imager. The whole-tumor specimen was reconstructed to measure the antibody distribution at the macroscopic level. (**F**) Antibody distribution heterogeneity measured in the reconstructed tumor specimen was significantly higher when MRI contrast heterogeneity of the same patient tumor was high. (**G**) ROC analysis showed that MRI contrast heterogeneity can predict antibody distribution heterogeneity. (Mann-Whitney test, error bar means standard deviation, * denotes $P<0.5$).